Reaction Chemistry & Engineering

ROYAL SOCIETY OF CHEMISTRY

PAPER

Cite this: *React. Chem. Eng.*, 2025, **10**, 1910

Performance of a gliding arc plasmatron pilot reactor with an integrated carbon bed and recirculation for upscaled CO_2 conversion†

Robbe Bryssinck, ‡*[abcd] Gregory James Smith, ‡[ab] Colin O'Modhrain, ‡[ab] Tom Van Assche, [c] Georgi Trenchev ‡[abd] and Annemie Bogaerts ‡[ab]

Received 29th April 2025,
Accepted 8th May 2025

DOI: 10.1039/d5re00190k

rsc.li/reaction-engineering

In this work, we investigated the performance of a multi-reactor gliding arc plasmatron (MRGAP) pilot reactor with an integrated carbon bed and recirculation. Experimentally, we varied the following parameters: carbon bed position, total flow rate, recirculation and a semi-continuous feeding system. The optimum operating conditions were found to be with the carbon bed located closest to the reactor outlets (35 mm) at a flow rate of 50 L min^{-1} with a semi-continuous carbon feed. Under these conditions, we obtain a maximum CO_2 conversion of 20%, corresponding to a conversion rate of 1068 g h^{-1} and a CO concentration of 33 vol% at the outlet. The plug-power based energy cost (EC) for these optimum conditions was 5.8 MWh t_{CO}^{-1} (1.2 MJ $mol_{CO_2}^{-1}$). When implementing a gas recirculation stage, the CO_2 conversion increases from 10.3% to 12.7%, but the EC rises from 10.9 MWh t_{CO}^{-1} to 13.7 MWh t_{CO}^{-1}. To complement the experimental work, we also developed a 2D model of the post-plasma chamber, coupled to a simple model for the plasma reactor. The model enables further insights into the effect of the carbon bed position and temperature on the performance, and confirms that when the carbon bed is positioned closer to the inlets, the performance increases. Both experimental and modelling results indicate that the integration of a carbon bed into an industrial scale plasma reactor is viable and can improve both the CO_2 conversion and energy metrics.

1. Introduction

The current focus on mitigating carbon emissions lies in carbon capture and storage (CCS) or carbon capture and utilisation (CCU) processes, where CCS aims for long-term carbon dioxide (CO_2) storage, whereas CCU utilizes CO_2 as a building block for value-added chemicals, such as e-fuels and polymers.[1,2] One method for converting CO_2 into its respective building blocks is *via* dissociation:

$$CO_{2(g)} \rightarrow CO_{(g)} + \frac{1}{2}O_{2(g)} \quad \Delta H° = +283 \text{ kJ mol}^{-1} \qquad (1)$$

This process faces two main challenges: i) the reaction is endothermic and thus requires high temperatures to be favourable[2] (starting from 2000 K at atmospheric pressure). ii) To be useful on an industrial scale, the exhaust gas from the reactor should be O_2-free.[3] When O and O_2 are produced in the process of CO_2 splitting, they can recombine with CO into CO_2, lowering the net CO_2 conversion.[3,4] Due to the first challenge, thermal CO_2 splitting is not industrially viable due to the high energy consumption required.

Clean energy technologies[2] aim to decarbonize and electrify chemical processes, such as the production of methanol or ammonia.[5] A promising pathway is plasma technology. In a plasma reactor, a reactive mixture of high-energy electrons, radicals, ions, and excited and neutral species can be generated by applying an electric field to a gas.[6,7] Plasma reactors can be operated under ambient conditions (atmospheric pressure) and can be rapidly switched on/off, making them compatible with renewable energy sources with variable output. Additionally, plasma technology eliminates the need for heating the gas as a whole, as plasma acts as a specific heat source due to Joule heating.[2]

Plasma-based CO_2 splitting has been extensively studied using various types of reactors. In this work, a gliding arc (GA) plasma reactor[8,9] is used. It operates at atmospheric pressure, so the CO_2 conversion proceeds *via* thermal

[a] *Research group PLASMANT, Department of Chemistry, University of Antwerp, Universiteitsplein 1, 2610 Wilrijk, Belgium.*
E-mail: robbe.bryssinck@uantwerpen.be; Tel: +32 (0)48 660 8482
[b] *Electrification Institute, University of Antwerp, Olieweg 97, 2020 Antwerp, Belgium*
[c] *Department of Chemical Engineering, Vrije Universiteit Brussel, Pleinlaan 2, 1050 Brussel, Belgium*
[d] *D-CRBN, Olieweg 95, 2020 Antwerp, Belgium*

† Electronic supplementary information (ESI) available: Additional details on the multidimensional model. See DOI: https://doi.org/10.1039/d5re00190k

‡ These authors share first authorship.

reactions.[8,10] The advantage of using a GA reactor is that it has a relatively low cost and simple design, and its operation at atmospheric pressure.

As mentioned above, CO_2 conversion by plasma leads to the production of O/O_2 species that can recombine with produced CO to reduce the net conversion, as well as increase the energy cost (EC). Note that the EC is defined as the specific energy input (SEI) divided by either the CO_2 conversion or the amount of CO produced, where the SEI is the power over the gas flow rate (see *e.g.*, definition in Snoeckx *et al.*[2] or eqn (5) below). One method of removing these species and reducing the rate of recombination reactions is by reaction with solid carbon. Such heterogeneous reactions increase the concentration of CO in the exhaust. Furthermore, at sufficiently high temperature, the unconverted CO_2 exiting the plasma reactor can also react with the solid carbon. This reaction is called the reverse Boudouard reaction (RBR):[4]

$$CO_{2(g)} + C_{(s)} \rightarrow 2CO_{(g)} \quad \Delta H^{\circ} = +172 \text{ kJ mol}^{-1} \tag{2}$$

This endothermic reaction requires elevated temperatures (>1000 K)[4,11] to proceed at an appreciable rate at atmospheric pressure. Prior work investigating the effect of the RBR has been conducted in several studies.[4,12–19] A comprehensive overview of these studies is shown in O'Modhrain *et al.*[13] In this paper, the authors observed that a higher specific energy input (SEI), and hence a higher power, increases the temperature of the hot plasma effluent in contact with the carbon bed. In addition, a functioning silo was implemented, which supplied fresh carbon to the bed and maintained the improved metrics on the order of 1 hour. These improvements lead to a sustained conversion of 41%, corresponding to a CO concentration of 58% and an EC of 0.41 MJ $mol_{CO_2}^{-1}$. Another more recent paper by PLASMANT, in collaboration with Zhejiang University,[12] also reported a CO_2 conversion above 40% at an EC below 2.8 eV per molecule or 0.28 MJ $mol_{CO_2}^{-1}$. This was achieved by improved coupling between the plasma and carbon bed, highlighting the benefit of moving the bed as close as possible to the plasma reactor outlet. In general, these results highlight the potential of placing a carbonaceous material after the plasma to boost the performance. It is important to note that the EC mentioned in the literature, *e.g.*, expressed in MJ $mol_{CO_2}^{-1}$, is often based on the plasma power, and thus focused on the amount of plasma energy that is consumed to convert CO_2, not taking into account the efficiency of the power supply. From an industrial point of view, it is more interesting to report the EC based on the plug power, thus accounting for the efficiency of the power supply and focusing on the amount of energy consumed to obtain a certain amount of product, in this case CO, *e.g.*, expressed in MWh t_{CO}^{-1}. In this work we focus on industrial applications, so we use the plug power to calculate the EC.

Another method commonly used in industry to increase conversion is the implementation of a recycling step, such as that conducted in the nitrogen-fixing Haber–Bosch process.[20] Here, the reactor outlet stream consists of produced ammonia (NH_3) with unreacted hydrogen (H_2) and nitrogen (N_2). The NH_3 is removed by separation and the unreacted components are mixed with a fresh feedstock and recycled back to the processing reactor.[21] While recycling units are very common in the chemical industry, their implementation into plasma-based technology is thus-far scarce. Vertongen *et al.*[22] studied the effect of recirculation flow by using a step-wise approach. The authors determined the CO_2, CO and O_2 output of a single reactor and fed a mixture with an identical composition into the same reactor, mimicking several reactors operating in series. This procedure was repeated until a plateau in conversion was reached. The authors demonstrated an increase in conversion with the number of passes, albeit at the cost of a rise in the EC. The latter could be largely mitigated, however, by combining the recycling with O_2 removal after each pass. In reality, placing multiple plasma reactors in series may be challenging for an industrial setting, as it is cost-intensive and requires more space to operate safely. Another challenge arises due to the tuning of the recycled gas flow to find an appreciable balance between the CO_2 conversion and the EC.

To gain additional insights and to attempt to unravel the underlying mechanisms of a post-plasma carbon bed, Girard-Sahun *et al.*[4] developed a zero-dimensional (0D) chemical kinetic model to study the contributions of different reactions occurring within such a carbon bed. The results revealed that the onset of oxygen coverage at the carbon surface is detrimental to the process performance. This occurs due to the selectivity towards CO_2 being increased *via* the $C_{(s)}$–O oxidation and the forward Boudouard reaction, resulting in a drop in CO_2 conversion and CO concentration. In addition, the formation of oxygen complexes on the surface of the carbon leads to passivation and hence deactivation of the carbon bed. Recent work by Biondo *et al.*[12] built further upon this kinetic model, with the authors investigating the effect of the distance between the plasma reactor outlet and carbon bed on the performance. This study revealed among others that the closer the carbon bed was placed to the plasma reactor outlet, the higher the temperature was in the bed, which increased the RBR rate. Interestingly, the simulation predicted that the carbon bed was in fact not chemically quenching the recombination reactions. Instead, if the temperature of the carbon bed exceeded 1500 K, the RBR increased the CO_2 conversion and compensated for the reduced conversion due to the recombination reactions. The authors also highlighted that the implementation of a post-plasma carbon bed is beneficial for setups with moderate conversion and heat losses to the reactor walls. In case of a reactor reaching high conversion, it is important to maintain higher temperatures at the carbon bed, to prevent oxidation, otherwise the positive effects of the carbon bed are lost.

In this work, we investigate the influence of several process parameters on the performance of a post-plasma

carbon bed implemented in a pilot-scale multi-reactor gliding arc plasmatron (MRGAP) reactor. We examined the influence of the flow rate, carbon bed position, and the introduction of a semi-continuous feeding system with interval zones. Additionally, we explored the effect of real-time effluent recycling, wherein a portion of the exhaust gas was reintroduced to the reactor with pure CO_2.

As mentioned above, recent modelling work investigating the role of reactions occurring within a carbon bed has been conducted only using 0D models. There are no existing higher dimensional models in the literature describing a post-plasma carbon bed. We therefore developed a 2D post-plasma chamber model consisting of both gas and solid phases, which monitors the ablation of solid carbon particles and the subsequent production of CO as a function of time. We examined the effect of the bed distance and temperature on the CO concentration in the exhaust region, which contributes to our interpretation of the experimental trends.

2. Experimental method

2.1. Experimental setup

The MRGAP pilot-scale reactor used in this work was developed by D-CRBN, a spin-off company of the research group PLASMANT. The reactor is placed inside a 10 ft container, together with other important process elements, such as power supplies, a heat pump/chiller, and the programmable logic computer (PLC), as shown in Fig. S1 in the ESI.†

Fig. 1a shows the pilot reactor, which consists of three main chambers: a pre-plasma chamber, a plasma chamber and a post-plasma chamber. The pre-plasma chamber is connected to the CO_2 gas input and contains the anode plate, with seven parallel GA reactor nodes.

Fig. 1a shows the total gas inlet and outlet, the pre- and post-plasma chambers, the position of the carbon feed and the three K-type thermocouples (T1–T3) used to measure the temperature of the gas leaving the plasma chamber. A more detailed view of the anode plate can be seen in Fig. 1b. It contains seven identical GAP reactor nodes (shown in detail in Fig. 1c) with a flange. These reactor nodes (*i.e.*, plasma chambers) consist of three main parts: a high voltage cathode (diameter = 18 mm, height = 19 mm), ceramic insulation (height = 2 mm), and a grounded anode (diameter = 20 mm, height = 18 mm). CO_2 (99.7%, Air Liquide) is introduced into the pre-plasma chamber through a singular inlet at a total flow rate of 50–110 L min^{-1}. The gas is then distributed over the seven reactor nodes and introduced *via* individual tangential inlets (diameter = 3.2 mm). The reactors are designed to enable the formation of a reverse-vortex flow stabilization pattern inside the node cavity.[23,24] The gas exits the reactor nodes through their respective gas outlet (diameter = 7 mm) into the post-plasma chamber (diameter = 170 mm, height = 470 mm). In the diagnostic box, the following sensors are placed: an optical O_2-sensor (FDO2, PyroScience GmbH) and two near-dispersive infrared (NDIR) sensors, one for CO_2 and the other for CO (FlowEvo, SmartGas).

The pre-plasma chamber (diameter = 170 mm, height = 280 mm) contains the high voltage connections, which serve as a link between the nodes and their respective power supply units (PSUs). The PSUs are switching-type high voltage generators with a negative output which drive arc plasmas with a power around 1 kW DC.

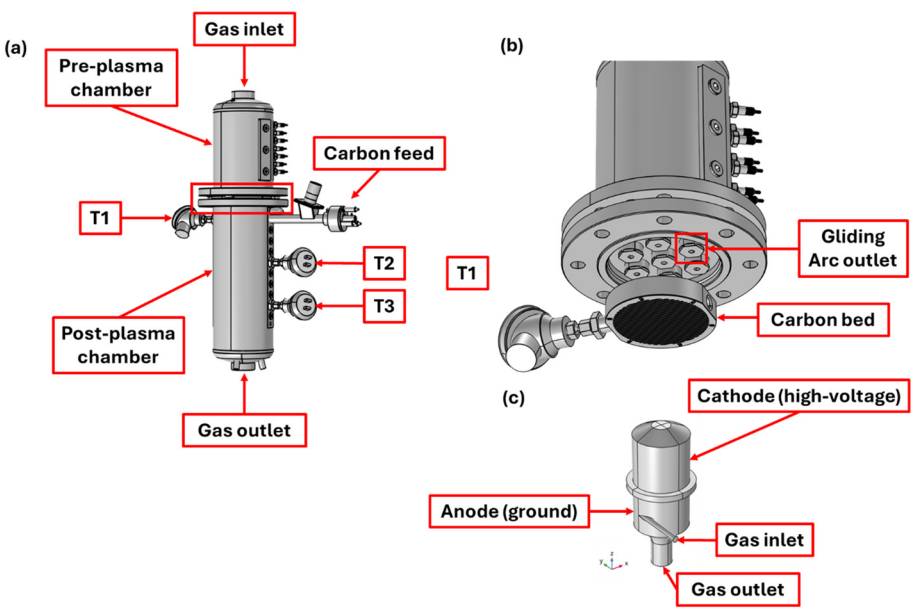

Fig. 1 3D renderings of the pilot reactor with (a) an overview of the system as a whole, (b) a more detailed view of the anode plate and carbon bed inside the post-plasma chamber and (c) a single GAP reactor node.

The post-plasma chamber is equipped with a fluid jacket for water cooling, enabled by a heat exchanger connected to a heat pump/chiller. Additionally, it houses the carbon bed (diameter = 136 mm, height = 27 mm, mesh number = 8) with connection points on the chamber wall. The presence of multiple connection points enables placing the carbon bed at different heights. The carbon bed consists of a stainless steel ring and a mesh plate.

Fig. 2 shows the P&ID of the D-CRBN pilot setup inside the container, with pressure sensors at the input and output gas lines (P1 and P2). Each sensor and control device are connected to the PLC. Furthermore, the pilot container is equipped with a carbon silo (to provide a continuous feed of fresh carbon), a heat pump/chiller (CH), and a recirculation stage/loop containing a check valve (CV), a ball valve (BV), a needle valve (NV), and a pump (P). The carbon is fed from the carbon silo into the carbon bed under the influence of a screw feeder, to ensure a controlled feeding rate during operation. A filter is mounted at the end of the post-plasma chamber to remove residual particulate matter. In the continuous feeding experiments, the flow rate was set at 50 L min^{-1} and 50 g of activated carbon (NORIT PK, 3–5 mm) was initially loaded in the bed. The reactor was tilted to a 25° angle relative to the vertical to ensure a good carbon spreading inside the carbon bed. For the recirculation stage, a recycling rate of 50% was selected. This represents the amount of output gas that is re-introduced to the reactor *via* the total inlet. As a consequence, the PLC system adjusts the inlet flow rate to maintain a steady input value. A picture of the setup can be found in the ESI† (section S1 and Fig. S2).

2.2. Performance metrics calculations

Previous studies have extensively and accurately defined methods for determining conversion, accounting for the "gas expansion" that occurs during reactions such as CO_2 splitting (*i.e.* 1 mole of reactant into 1.5 mole of products).[25,26] In these studies, one approach to calculate the conversion X (%) is by using the inlet and outlet volumetric flow rates of the gases. This is done *via* the following formula:[24,25]

$$X\ (\%) = \frac{Q_{in} - Q_{out} \cdot y_{CO_2}^{out}}{Q_{in}} \cdot 100 \quad (3)$$

with Q_{in} (L min^{-1}) and Q_{out} (L min^{-1}) representing the volumetric flow rates at the inlet and outlet, respectively, and y being the fraction of the component indicated in the subscript detected in the effluent. To calculate Q_{out}, the oxygen balance is utilized as defined in previous studies:[4,15]

$$Q_{out} = \frac{2 \cdot Q_{in}}{\left(2 \cdot \left(y_{CO_2}^{out} + y_{O_2}^{out}\right) + y_{CO}^{out}\right)} \cdot 100 \quad (4)$$

Besides conversion, also the EC is an important performance metric. In our work, it is expressed in kWh t_{CO}^{-1} produced, defined as:

$$EC = \frac{P \cdot V_m}{60 \cdot M_{CO} \cdot Q_{out} \times y_{CO}} \cdot 1 \times 10^6 \quad (5)$$

where P (kW) represents the power (plug power in our case), V_m (L mol^{-1}) is the molar volume at atmospheric pressure and room temperature (24.06 L mol^{-1}), M_{CO} (g mol^{-1}) is the molar mass of CO, the factor 60 is to convert min to hours, and the factor 1×10^6 is to convert grams to tonnes.

It is important to note that the EC in this work is calculated with respect to the plug power (*i.e.* the total power of the system), which is important for assessing the industrial potential. Therefore, this value should not be compared directly with EC values from the literature, wherein the use of the plasma-deposited power is commonly used to determine energy metrics. Generally, the plasma power is 60–

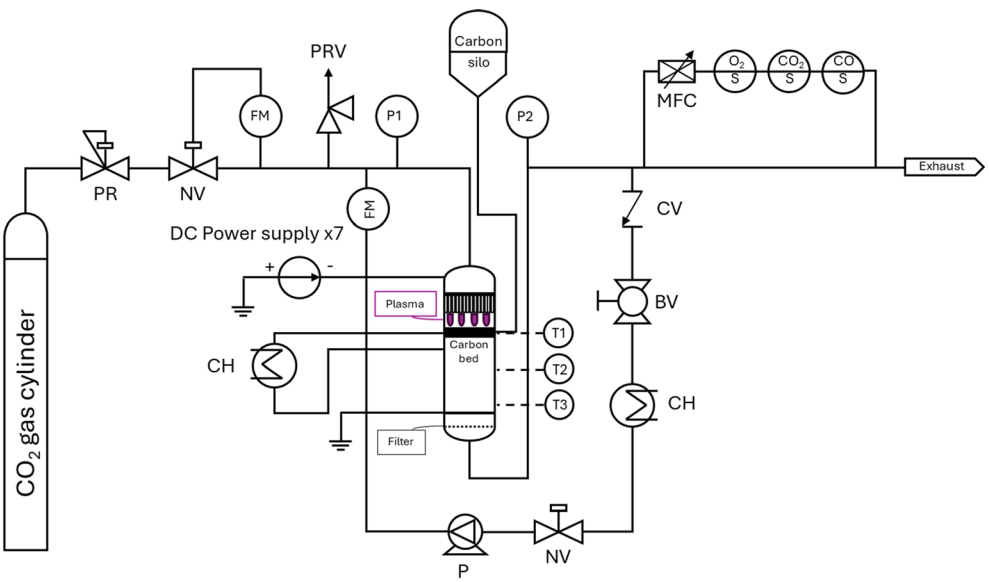

Fig. 2 P&ID of the D-CRBN pilot setup.

80% of the plug power, which makes the EC value based on plasma power clearly lower.

Finally, the conversion rate (CR) (g h^{-1}) is calculated as follows:[27]

$$CR = \frac{Q_{in} \cdot X \cdot 60 \cdot M_{CO_2}}{V_m \cdot 100} \quad (6)$$

where M_{CO_2} (g mol^{-1}) is the molar mass of CO_2.

Except where explicitly stated, all measurements have been performed in triplicate and error bars have been calculated by using the standard deviation.

3. Model description of the post-plasma carbon bed

We developed a multi-dimensional post-plasma chamber model, consisting of a gas phase (before and after the carbon bed) and a porous medium (in the carbon bed), coupled to a simple CFD plasma reactor model (providing input to the post-plasma chamber model), using COMSOL Multiphysics (version 6.2).

We applied a step-wise process of model development in order to explore the system as a whole. This approach has been utilised in previous studies,[28,29] and is implemented to reduce the computational cost of simulating the system as a whole (plasma reactor and post-plasma chamber with a carbon bed). Initially, we solve a 3D fluid flow model of a single GAP reactor (*i.e.* plasma chamber) and we extract radially-averaged velocity profiles (Fig. S3 and S4 in the ESI†). These profiles are implemented as inlet boundary conditions for a 2D axisymmetric model of a single GAP reactor (Fig. S5†). In this stage, we approximate the plasma by a uniform heat source, with the applied power matching the experimental values (Fig. S6†). From this model, we extract the outlet gas temperature and velocity profiles (Fig. S7†), to be applied to the final stage. This final stage simulates the post-plasma chamber (Fig. 3) as a 2D slice, wherein the outlets of multiple GAP reactors are fed into a single domain, either with or without a carbon bed region.

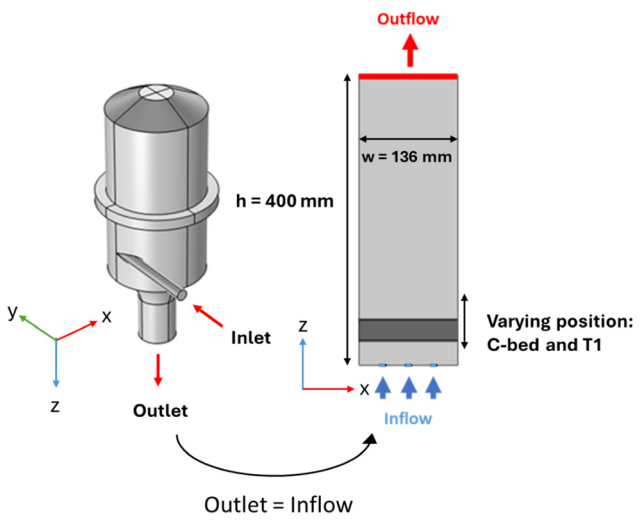

Fig. 3 3D geometry of a single plasma chamber (MRGAP reactor node; left) and 2D geometry of the post-plasma chamber (right), where the plasma chamber outlet corresponds to the inflow of the post-plasma chamber. The three gas inlets, the carbon bed, and the outlet are indicated, as well as the dimensions of the post-plasma chamber.

The primary focus of this work is the post-plasma chamber region and the effect of the carbon bed on the gas dynamics therein. As such, we will discuss the 2D post-plasma chamber model in detail, while the simulations for deriving the inlet velocity and temperature profiles (3D and 2D axisymmetric GAP simulations) can be found in the ESI† (sections S2 and S3), as explained in the previous paragraph.

3.1. Geometry

The link between the plasma chamber and the 2D modelling domain of the post-plasma chamber is shown in Fig. 3, including the domain dimensions and carbon bed location(s).

The post-plasma chamber simulation domain represents a slice of the 3D reactor exhaust through three plasma chamber (MRGAP reactor node) outlets (*cf.* Fig. 1b), resulting in the three gas inlets in Fig. 3. The rectangular simulation domain is 400 mm long and 136 mm wide, with an out-of-plane thickness (d_y) of 7 mm (assuming homogeneity in this dimension). This value for d_y is chosen to align with the diameter of the plasma chamber outlets, and to better approximate the flow rate. The individual inlets have a width of 7 mm, matched to the diameter of the plasma chamber outlets. To compare with our experiments, three distinct conditions are investigated: no carbon bed, a carbon bed in position 1 (35 mm from the inlets) and in position 2 (65 mm from the inlets). Other carbon bed positions were also investigated, namely 45 mm and 55 mm from the inlets.

The model domain discretization was refined until convergence, with the number of mesh elements ranging between 67 859 and 107 710. A range for the number of mesh elements is required due to the nature of each individual simulation, where the location of the carbon bed alters the number of elements required and is mostly affected by the pre-bed area requiring a higher resolution than the post-bed region. A table with the number of mesh elements per simulation can be found in the ESI† (section S4). The boundary conditions of the model can also be found in the ESI† (section S5).

3.2. Equations

3.2.1 Navier–Stokes equation and the Brinkman approximation. In the post-plasma chamber, the gas phase fluid modelling before and after the carbon bed region is carried out using the Navier–Stokes equation:[30]

$$\rho \frac{\partial \boldsymbol{u}}{\partial t} = \nabla \cdot \left[-p\boldsymbol{I} + \mu\left(\nabla \boldsymbol{u} + (\nabla \boldsymbol{u})^T\right) - \frac{2}{3}\mu(\nabla \cdot \boldsymbol{u})\boldsymbol{I} \right] + \boldsymbol{F} \quad (7)$$

where ρ (kg m^{-3}) is the density of the gas, $\boldsymbol{u}$ (m s^{-1}) is the velocity vector, p (Pa) is the pressure, μ (kg m^{-1} s^{-1}) is the dynamic viscosity of the fluid, superscript T describes

transposition, $\boldsymbol{I}$ is the unity tensor, and $\boldsymbol{F}$ (N m^{-3}) the external forces applied to the gas.

In the carbon bed region, the flow through the porous medium is described by the Brinkman approximation:[30]

$$\frac{\rho}{\varepsilon_p}\frac{\partial \boldsymbol{u}}{\partial t} = -\nabla p + \nabla\cdot\left[\frac{1}{\varepsilon_p}\left\{\mu\left(\nabla\boldsymbol{u} + (\nabla\boldsymbol{u})^T\right) - \frac{2}{3}\mu(\nabla\cdot\boldsymbol{u})\boldsymbol{I}\right\}\right] - \left(\kappa^{-1}\mu + \frac{Q_m}{(\varepsilon_p)^2}\right)\boldsymbol{u} + \boldsymbol{F} \quad (8)$$

where ε_p is the porosity, κ (m^2) is the permeability of the porous medium, and Q_m (kg m^{-3} s^{-1}) is a mass source term.

The gas flow through the porous medium assumes non-Darcian flow, due to the temporally varying nature of the bed porosity and the requirement to calculate permeability continuously. The permeability and porosity are self-consistently solved throughout the simulation and the equations for this can be seen in section 3.2.4 below.

3.2.2 Heat balance equation. The temperature within the post-plasma chamber is determined by the thermal balance equation, which is defined in the porous medium and fluid domains separately. We assume that the porous medium reaches a local thermal equilibrium between solid and gas, meaning that solid and gas are treated as a single material at a single temperature in this region. The heat balance equation for the post-plasma chamber gas domain (before and after the porous medium) is given as:

$$d_y\rho C_p\frac{\partial T}{\partial t} + d_y\rho C_p\boldsymbol{u}\cdot\nabla T + \nabla\cdot\boldsymbol{q} = d_y Q \quad (9)$$

with:

$$\boldsymbol{q} = -d_y k\nabla T \quad (10)$$

and:

$$Q = -r\cdot H \quad (11)$$

where Q (W m^{-3}) is the heat of reaction, r (mol m^{-3} s^{-1}) is the reaction rate, and H (kJ mol^{-1}) is the enthalpy of the reaction (in our case +172.5 kJ mol^{-1}).

The gas density ρ is calculated using the ideal gas law:

$$\rho = \frac{pM_n}{R_g T} \quad (12)$$

Here, d_y (m) is the out-of-plane thickness (explained above), C_p (J kg^{-1} K^{-1}) is the heat capacity of the gas, T (K) is the temperature, q (W m^{-2}) is the conductive heat flux, k (W m^{-1} K^{-1}) is the thermal conductivity of the gas, M_n (g mol^{-1}) is the mean molar mass of the gas, and R_g (m^3 Pa K^{-1} mol^{-1}) is the gas constant.

The heat balance equation in the porous medium is defined as:

$$d_y(\rho C_p)_{\text{eff}}\frac{\partial T}{\partial t} + d_y\rho_f C_{p,f}\boldsymbol{u}\cdot\nabla T + \nabla\cdot\boldsymbol{q} = d_y Q \quad (13)$$

with:

$$(\rho C_p)_{\text{eff}} = \varepsilon_p\rho_f C_{p,f} + \theta_s\rho_s C_{p,s} \quad (14)$$

and:

$$\boldsymbol{q} = -d_y k_{\text{eff}}\nabla T \quad (15)$$

The thermal conductivity coefficient, k_{eff}, is determined for spherical particles distributed homogeneously and is defined as:

$$k_{\text{eff}} = k_f\frac{(2k_f + k_s - 2(k_f - k_s)\theta_s)}{2k_f + k_s + (k_f - k_s)\theta_s} + k_{\text{disp}} \quad (16)$$

where ρ_f (kg m^{-3}) is the fluid density, ρ_s (kg m^{-3}) is the solid density, $C_{p,f}$ (J kg^{-1} K^{-1}) is the heat capacity at constant pressure for the fluid, $C_{p,s}$ (J kg^{-1} K^{-1}) is the heat capacity at constant pressure for the solid, k_{eff} (W m^{-1} K^{-1}) is the effective thermal conductivity in the porous medium, k_f (W m^{-1} K^{-1}) is the thermal conductivity of the fluid, k_s (W m^{-1} K^{-1}) is the thermal conductivity of the solid, θ_s is the volume fraction of the solid, and k_{disp} (W m^{-1} K^{-1}) is the dispersive thermal conductivity.

3.2.3 Species transport equations. The transport of species in the gas phase domain of the post-plasma chamber is defined using the conservation of mass:

$$\rho\frac{\partial\omega_i}{\partial t} + \nabla\cdot\boldsymbol{j}_i + \rho(\boldsymbol{u}\cdot\nabla)\omega_i = R_i \quad (17)$$

Here, ω_i is the weight fraction of species i, $\boldsymbol{j}_i$ (mol m^{-2} s^{-1}) is the diffusive flux vector of species i, and R_i (mol m^{-3} s^{-1}) is the total net production rate of species i.

$\boldsymbol{j}_i$ is derived from the mixture-averaged diffusion model:

$$\boldsymbol{j}_i = -\left(\rho D_i^m\nabla\omega_i + \rho\omega_i D_i^m\frac{\nabla M_n}{M_n} - \boldsymbol{j}_{c,i} + D_i^T\frac{\nabla T}{T}\right) \quad (18)$$

with D_i^m (m^2 s^{-1}) representing the diffusion coefficient for species i, $\boldsymbol{j}_{c,i}$ (mol m^{-2} s^{-1}) is the multi-component diffusive flux correction term, and D_i^T is the thermal diffusion coefficient (kg m^{-1} s^{-1}).

D_i^m, M_n, and $\boldsymbol{j}_{c,i}$ are calculated *via*:

$$D_i^m = \frac{1-\omega_i}{\sum_{k\neq i}\frac{x_k}{D_{i,k}}},\quad M_n = \left(\sum_i\frac{\omega_i}{M_i}\right)^{-1},\quad \boldsymbol{j}_{c,i} = \rho\omega_i\sum_k\frac{M_i}{M_n}D_k^m\nabla x_k \quad (19)$$

where x_k is the molar fraction of species k, $D_{i,k}$ (m^2 s^{-1}) is the multi-component Maxwell–Stefan diffusivity, M_i (g mol^{-1}) is the molar mass of species i, and D_k^m (m^2 s^{-1}) is the mixture-averaged diffusion coefficient for species k. The transport of species within the carbon bed is defined by the conservation of mass with additional terms:

$$\varepsilon_p\rho\frac{\partial\omega_i}{\partial t} + \nabla\cdot\boldsymbol{j}_i + \rho(\boldsymbol{u}\cdot\nabla)\omega_i = R_i + M_i\frac{\partial c_{\text{surf},i}}{\partial t}S_{\text{area}} \quad (20)$$

where S_{area} (m^{-1}) is the surface area ratio between the surface and gas volume in the bed, and $c_{\text{surf},i}$ (mol m^{-2}) is the surface concentration of species i.

The diffusive species flux ($\boldsymbol{j}_i$) is given as:

$$\boldsymbol{j}_i = -\left(\rho D_i^m \nabla\omega_i + \rho\omega_i D_i^m \frac{\nabla M_n}{M_n} - \boldsymbol{j}_{c,i} + D_{e,i}^T \frac{\nabla T}{T}\right) \quad (21)$$

with $D_{e,i}^T$ (kg m^{-1} s^{-1}) being the effective thermal diffusion coefficient for species i.

$$D_{e,i}^T = f_e(\varepsilon_p, \tau_F) D_i^T \quad (22)$$

where τ_F is the tortuosity.

D_i^m, M_n, and $\boldsymbol{j}_{c,i}$ are calculated *via*:

$$D_i^m = \frac{1-\omega_i}{\sum_{k\neq i}\frac{x_k}{D_{e,ik}}}, \quad M_n = \left(\sum_i \frac{\omega_i}{M_i}\right)^{-1}, \quad \boldsymbol{j}_{c,i} = \rho\omega_i \sum_k \frac{M_i}{M_n} D_k^m \nabla x_k \quad (23)$$

with

$$D_{e,ik}^T = f_e(\varepsilon_p, \tau_F) D_{ik} \quad (24)$$

3.2.4 Particle diameter and porosity. A partial differential equation (PDE) is implemented to describe the rate of change in particle diameter over time:

$$\frac{\partial d_p}{\partial t} = \frac{2R_{s,j}}{\rho_s} \quad (25)$$

where d_p (m) is the particle diameter, $R_{s,j}$ is the surface rate expression from the surface reaction (kg m^{-2} s^{-1}) for species j, and ρ_s is the solid density of the pellets (kg m^{-3}). Within the porous domain, the particles are assumed to be arranged as a 3D stack of spherical pellets. As can be seen in Fig. 4, the drop in particle diameter increases the porosity and permeability (assuming that the particles are stacked inside unit cells and do not move as their size decreases).

The porosity, ε_p, is defined by dividing the volume of the void space, V_v, by the total volume of the unit cell, V_{tot}:

$$\varepsilon_p = \frac{V_v}{V_{tot}} \quad (26)$$

The volume of the void space is calculated by subtracting the volume of the spherical particle ($V_{particle}$) from the total volume (V_{tot}), *cf.* Fig. 4. The volume of the void fraction is calculated by the following equation:

$$V_v = V_{tot} - V_{particle} = (d_p)^3 - \frac{4}{3}\pi\left(\frac{d_p}{2}\right)^3 \quad (27)$$

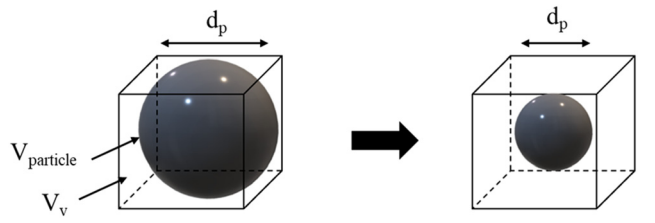

Fig. 4 Illustration of the change in size of a carbon particle inside a unit cell (simple cubic packing fraction).

The particle diameter and porosity are linked to the permeability (κ) of the carbon bed, which is calculated using the Ergun equation for spherical pellets:

$$\kappa = \frac{(d_p)^2}{150}\frac{(\varepsilon_p)^3}{(1-\varepsilon_p)^2} \quad (28)$$

3.3. Modeled conditions

The model assumes a CO_2/CO gas mixture where the gas properties are determined from the individual properties of the CO_2 and CO molecules, and the bulk gas properties from the interaction of these two molecules.[31,32] We do not consider plasma-specific radicals due to recent insights from a global model where O radicals react rapidly in the post-plasma regions such that we can neglect the inclusion of O.[12] In the experimental setup, the carbonaceous material loaded in the bed is consumed during plasma operation. This change results in the reduction of particle diameter while concurrently increasing the bed porosity. To capture this process in the simulation, we include a simplified version of the RBR (eqn (2)) in the model, solely focused on the rate of formation of gas phase CO from solid phase carbon. This rate is described with a rate coefficient (s^{-1}) given as:[33]

$$k\ (s^{-1}) = (4.85\times10^8)\cdot\exp\left(-\frac{E_a}{RT}\right)\cdot\frac{S_A}{S_{A_0}} \quad (29)$$

where 4.85×10^8 is the pre-exponential factor (s^{-1}), E_a is the activation energy (160.7 kJ mol^{-1}), R is the universal gas constant (8.314 J K^{-1} mol^{-1}), and T (K) is the temperature. To account for the change in the reaction rate with changing size of the particle, the rate is multiplied by the ratio of the surface area of the particles compared to their initial surface area, here given as S_A and S_{A_0}. To account for the endothermic nature of this reaction, a heat loss term is included in the heat balance equation, with a value equal to the reaction enthalpy of the RBR (eqn (2)).

The carbon bed is represented by a porous medium in the model and is assigned the parameters shown in Table 1.

We assume that the pellets have no internal porosity and the values for the solid pellet density and the heat capacity are taken from the literature.[34,35] The porosity of the carbon bed is calculated self-consistently (eqn (26)), which determines the porous bed density and heat capacity. The thermal conductivity of the carbon pellets is strongly influenced by internal porosity. In order to better capture the thermal properties of the carbon

Table 1 Carbon bed parameters

Parameter	Value
Initial particle diameter, d_p (mm)	5
Thermal conductivity, k (W m^{-1} K^{-1})	$0.15/\varepsilon_{p0}$
Carbon particle density, ρ_s (kg m^{-3})	2260
Carbon particle heat capacity, C_p (J kg^{-1} K^{-1})	710
Surface site concentration (mol m^{-2})	1×10^{-5}

bed with respect to the thermal conductivity, we assumed an initial value taken from experimental measurements, *i.e.* 0.15 W m^{-1} K^{-1}.[36] As this experimental value does not account for the void space, we have included the influence of porosity on the thermal conductivity using the initial porosity, ε_{p0}. After this, the thermal conductivity is calculated for the bed as defined in eqn (16). The surface site concentration of the carbon bed, $C_{(s)}$, is assumed to be constant, as determined for a similar carbon pellet material.[4] The surface area of the spherical pellets is calculated self-consistently from the diameter of the pellets.

4. Results and discussion

We experimentally investigated the effect of carbon bed positioning, the applied flow rate, a recirculation stage, and semi-continuous solid carbon feeding on the measured CO concentration, CO_2 conversion and EC.

4.1. Effect of the carbon bed position

We investigated two different carbon bed positions, namely 35 mm and 65 mm from the MRGAP reactor anode plate (termed position 1 and position 2, respectively). In each experiment, the total inlet flow rate was fixed at 70 L min^{-1} and an average power of 8.5 kW was applied over the 7 active GA reactors. The temperature was measured with thermocouples at three different positions along the reactor body, where 0 mm corresponds to the outlet of the plasma chamber. T1 was positioned centrally inside the carbon bed (and therefore moves with the carbon bed position), T2 at 155 mm and T3 at 275 mm.

In Fig. 5a, the CO concentration is plotted as a function of time for both bed positions and a benchmark test without a carbon bed. It is clear that position 1, being the closest to the anodes, exhibits the best performance. It can reach a CO concentration value up to 27 vol%, while for position 2, the CO concentration reaches a maximum of 15 vol%. This is better than the benchmark, which achieves a maximum CO concentration of 12 vol%. It is logical that the carbon bed position closest to the anodes, and thus to the plasma afterglow, yields the best performance, due to the higher temperature promoting the (endothermic) RBR. This can be seen in Fig. 5b, where the average temperature within the carbon bed is shown at T1 for the three cases. The temperature in the carbon bed (T1) is higher for position 1 (1400 K) than for position 2 (1200 K). The benchmark test showed only a temperature of 940 K within the empty bed, due to the extensive cooling of the gas by the water-cooled reactor walls.

Fig. 6 demonstrates that the conversion decreases by a factor of two upon moving the bed further from the plasma chambers, from *ca.* 16% (CR of 1176 g h^{-1}) at position 1, to 8% (CR of 601 g h^{-1}) at position 2. As a consequence, the EC nearly doubles, from 5.6 MWh t_{CO}^{-1} (position 1) to *ca.* 11 MWh t_{CO}^{-1} (position 2). This illustrates the importance of the carbon bed temperature for the reaction performance. It can be noted that a carbon bed even closer to the reactor outlets than 35 mm may yield better results, but this is not possible in our current setup due to a destabilising effect of the carbon and/or bed on the plasma arcs. These results, and the relative improvement when compared to the benchmark test, highlight the significance of placing the carbon bed as close as possible to the plasma for improving the CO_2 conversion (and thus CO concentration) and EC of the process.

4.2. Effect of the flow rate

Fig. 7 presents the measured CO concentration as a function of time, and the average temperatures at the three thermocouple positions, for three different flow rates. In each experimental run, 50 g of carbon was loaded into the bed.

As shown in Fig. 7a, the CO concentration decreases with increasing flow rate. At a flow rate of 70 L min^{-1}, the CO concentration reaches a peak value of 27 vol%, while at 90 L min^{-1} and 110 L min^{-1}, it reaches 22 and 14 vol%, respectively. These lower peak values are attributed to the fact

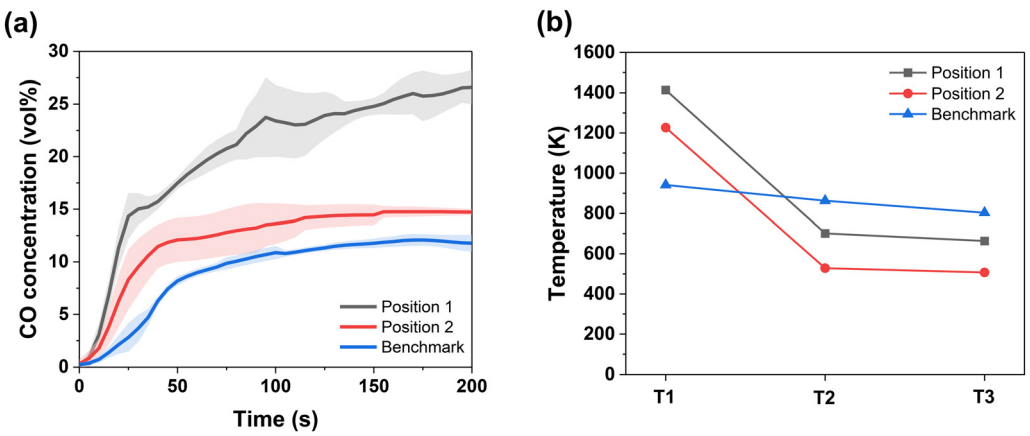

Fig. 5 (a) CO concentration (vol%) detected at the outlet as a function of time (s) for two carbon bed positions and a benchmark (without a carbon bed). (b) Average temperature (K) measured using three separate thermocouples at different positions in the post-plasma reactor (see text). The flow rate is fixed at 70 L min^{-1}.

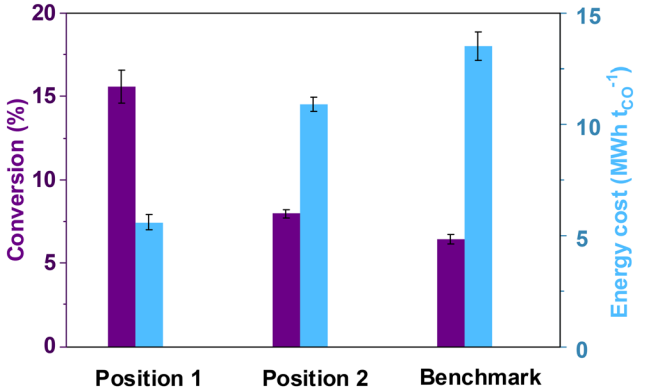

Fig. 6 CO_2 conversion (%) and energy cost (MWh t_{CO}^{-1}) in the presence of a carbon bed at position 1 (35 mm), position 2 (65 mm), and the benchmark (without a carbon bed) with a constant plug power of 8.5 kW and a flow rate of 70 L min^{-1}.

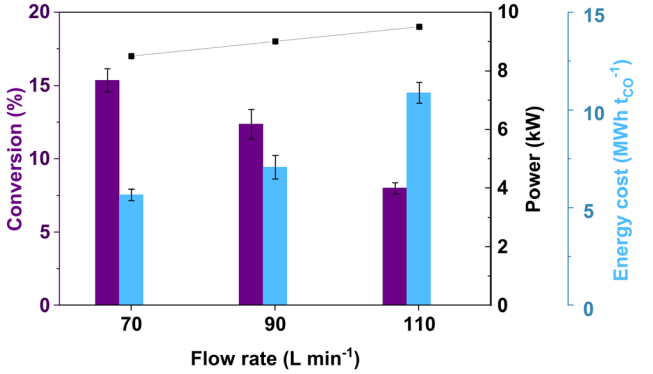

Fig. 8 CO_2 conversion (%), plug power (kW), and energy cost (MWh t_{CO}^{-1}) for the three different flow rates in the presence of a carbon bed at position 1 (35 mm).

that a higher flow rate yields a shorter residence time of the gas inside the carbon bed, in addition to enhanced cooling of the bed by the gas flow. The reduction in average bed temperature is confirmed by the temperature measurements shown in Fig. 7b. The temperature drops with increasing flow rate, thus reducing the efficiency of the RBR, which takes place in the carbon bed (T1). Furthermore, it can be seen that the CO concentration drops near the end of the experiment at 90 L min^{-1} and 110 L min^{-1}. Due to the lower temperature, the RBR does not compensate for the detrimental effects of the recombination reactions of O/O_2 on the performance. In addition to this, the O/O_2 species can form oxygenate complexes on the carbon surface, which lead to a decrease in performance.[12]

In terms of conversion, as shown in Fig. 8, a trend similar to that observed with CO concentration can be noticed as a function of increasing flow rate. The conversion drops from 15% at 70 L min^{-1}, to 12% at 90 L min^{-1}, and further to 8% at 110 L min^{-1}. Interestingly, as the decrease in absolute conversion is proportional to the increase in flow rate, the conversion rate is relatively constant between 70 and 90 L min^{-1}, with a value of around 1160 g h^{-1}. However, this proportionality does not hold true upon increasing to 110 L min^{-1}, as the CR drops to *ca.* 950 g h^{-1}. Consequently, the drop in conversion upon increasing the flow rate causes the EC to increase between 70 L min^{-1} and 90 L min^{-1}, from 5.6 MWh t_{CO}^{-1} to 7 MWh t_{CO}^{-1}. Further increasing the flow rate to 110 L min^{-1} results in the highest EC, with a value of around 11 MWh t_{CO}^{-1}. While the volumetric outflow of CO is similar between the different flow rates, the power increases from 8.5 kW at 70 L min^{-1} to 9 kW at 90 L min^{-1} and even further to 9.5 kW at 110 L min^{-1}. This increased power deposition leads to an increase in the EC as a function of flow rate. In addition, the pressure rises with increasing flow rate due to the flow constriction created by the carbon bed, resulting in an increased voltage and hence power.[37] In general, the results show that a higher flow rate causes a drop in CO concentration and CO_2 conversion, while the EC increases. These trends can again be attributed to the lower temperature in the carbon bed, making the RBR less favourable. Hence, it is advisable to work at lower flow rates, although a minimum flow rate is needed for stable plasma.

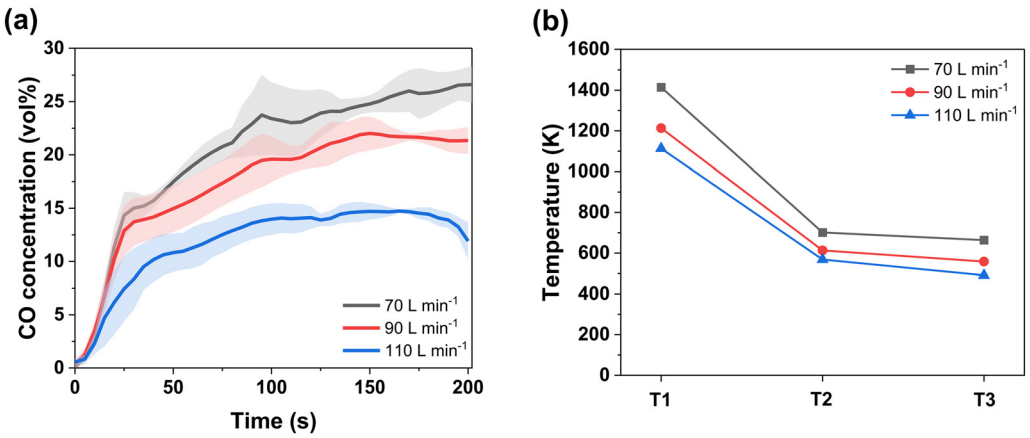

Fig. 7 (a) CO concentration (vol%) detected at the outlet as a function of time (s) and (b) average temperature (K) measured using three thermocouples at different positions in the post-plasma reactor (see text), for three different flow rates and a carbon bed at position 1 (35 mm).

4.3. Effect of a recirculation stage

Previous work highlighted gas recirculation in combination with O_2 removal as a potential avenue for boosting the overall CO_2 conversion.[22] Thus, we implemented a gas recirculation stage in combination with a carbon bed in the MRGAP reactor. We applied a flow rate of 50 L min^{-1} and a total plug power of 8.5 kW before activating the recirculation stage. This total power increased to 9.5 kW once gas recirculation was activated, due to an additional compressor required to add the recycled gas to the reactor inlet. The recirculation stage was initiated after 280 s and the recycling rate was set at 50%. The experiment was carried out with a different kind of carbon than all the other tests.

Fig. 9 demonstrates the positive effect of recirculation on the CO concentration, showcasing a rise in concentration once the recycling is activated (*ca.* 280 s). Indeed, the CO concentration rises from about 19 vol% to 23 vol%. This increase is due to unconverted CO_2 being recycled from the outlet to the inlet and subsequently converted into CO. While some of the CO formed in the initial pass will be destroyed within the plasma reactor during the recycling stage, the net CO output increases upon activation of the recycling stage. The presence of a carbon bed filled with a carbonaceous material ensured that the O_2 concentration detected in the effluent over the course of the experiments was below 1 vol%.

Fig. 10 shows that the conversion increases from 10% (CR of 555 g h^{-1}) to 13% (CR of 687 g h^{-1}), while the EC also rises from 10.9 MWh t_{CO}^{-1} to 13.7 MWh t_{CO}^{-1}. The increase in the EC is attributed to two parameters: power and input flow rate. The power increases by 1 kW when the recirculation stage is activated due to the additional compressor required to combine the recycled flow with the fresh input. At our

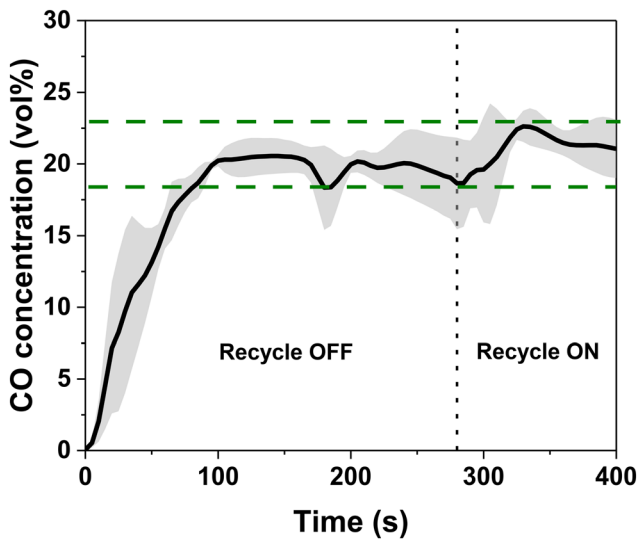

Fig. 9 CO concentration (vol%) detected at the outlet as a function of time (s), with a recirculation stage after 280 s and a recycling rate of 50%, in the presence of a carbon bed at position 1 (35 mm) and a total flow rate of 50 L min^{-1}.

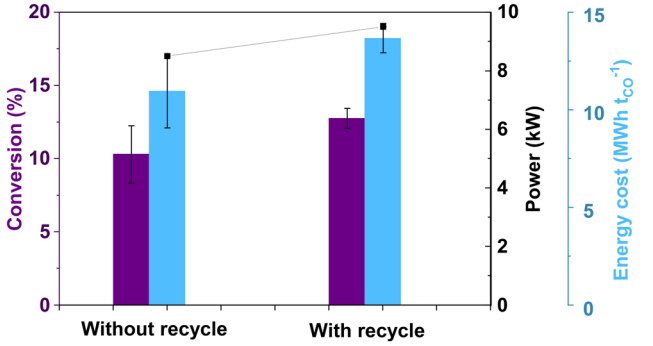

Fig. 10 CO_2 conversion (%), plug power (kW), and energy cost (MWh t_{CO}^{-1}) without and with a recirculation stage, at a recycling rate of 50%, in the presence of a carbon bed at position 1 (35 mm) and with a flow rate of 50 L min^{-1}.

selected recycling rate, the fresh input flow rate (*i.e.* pure CO_2) is reduced by 50%. As the initial input flow rate is set to 50 L min^{-1}, the new fresh input flow rate drops to 25 L min^{-1} while an equal amount of effluent gas is recirculated. If the additional conversion achieved is lower than the extra energy needed, the EC rises. As this is the case in our reactor, it is evident that the recirculation stage has a positive effect on the CO concentration and the CO_2 conversion, and a negative effect on the EC. Note that the EC is based primarily on two variables, the power and the CO output (see eqn (5)). When comparing the conversion (and hence the CO concentration and output) of Fig. 7 and 9, it is lower in Fig. 9, at the lower flow rate (*i.e.* recirculation experiments prior to the recirculation stage being implemented), which explains the higher EC. We specifically note that despite the inlet mixture being different between the two stages, the overall CO_2 conversion benefits from the recycling stage. These results are in line with the previous work of Vertongen *et al.*,[22] and repeated recycling would likely further improve conversion at the expense of the EC. Note that the heat exchanger reduces the exhaust gas temperature before it recirculates to remain within the temperature boundaries of the flow meter. Not doing this however could lead to a higher conversion, due to the higher temperature of the inlet gas. However, the current setup does not feature a temperature measurement of the recycled gas stream, as can be seen from the P&ID. Therefore, we cannot correlate the temperature of the recycled gas stream with the performance of the reactor at this moment.

4.4. Effect of semi-continuous feeding

To overcome the limitations of carbon consumption/deactivation outlined in previous work,[4] we implemented a semi-continuous carbon feeding system. The influence of carbon feeding on the CO output, CO_2 conversion and EC is presented in Fig. 11 and 12. In contrast to the previous results, which were reported from triplicate experiments, this behaviour of CO concentration as a function of time was obtained from a single run.

The protocol was based on a period of 2 minutes of operation, followed by a feeding interval of 1 minute, which

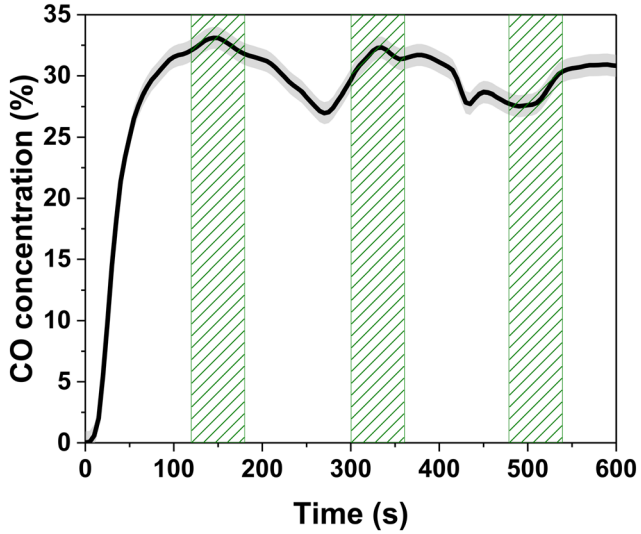

Fig. 11 CO concentration (vol%) detected at the outlet as a function of time (s) with three marked feeding intervals of 60 s every 2 min, with a carbon bed at position 1 (35 mm) and a flow rate of 50 L min^{-1}.

was repeated several times. Fig. 11 illustrates that the CO concentration initially increases to a value of 33 vol% due to reactions occurring in the pre-filled carbon bed. If no extra carbon is supplied, the CO concentration would decrease after some time as the carbon within the bed is consumed. This can be avoided by feeding extra carbon. After the first feeding interval, the temperature within the bed drops from 1400 to 1300 K due to the introduction of cold carbon. This in turn reduces the efficiency of the RBR, which manifests as a drop in CO concentration from 33 vol% to 27 vol% (from 180 s to 260 s). Once the bed temperature is raised by the hot plasma reactor effluent, the CO concentration increases again to a value of 32 vol%. This same trend of decreasing and increasing CO concentration is observed again after the second interval. In this instance, the decline in CO production is less noticeable compared to the previous interval, likely due to the fact that 'cold' carbon fed into the reactor is slowly heated during operation, as the solid carbon

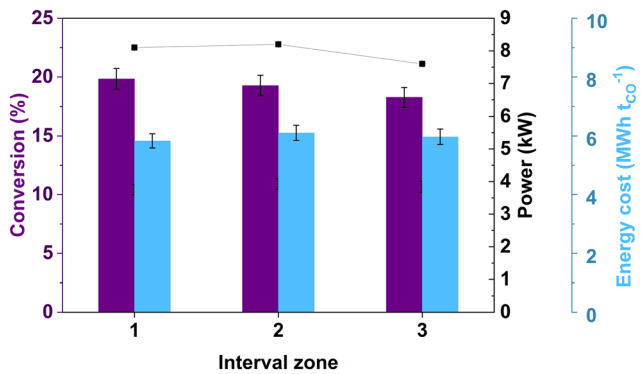

Fig. 12 CO_2 conversion (%), plug power (kW), and energy cost (MWh t_{CO}^{-1}) with three marked feeding intervals of 60 s after every 2 min, with a carbon bed at position 1 (35 mm) at a flow rate of 50 L min^{-1}.

feeding line and silo are not completely isolated from the post-plasma chamber.

Fig. 12 shows the conversion, plug power and EC, after each time interval (of 120 s operation and 60 s feeding), *i.e.* at 180, 360 and 540 s. The values remain relatively constant after feeding carbon into the carbon bed, although the conversion decreases slightly over time, from 20% during interval 1, to 19% through interval 2 and finally to 18% after interval 3. Naturally, when the CO concentration drops between the feeding intervals, a decrease in conversion occurs. As stated above, this can be attributed to the temperature not equilibrating between the gas and the carbon inside the bed. Furthermore, the power fluctuated during the experiment from 8.1 kW (interval 1) to 8.2 kW (interval 2) and 7.6 kW (interval 3). As a consequence, the EC changes slightly from 5.8 MWh t_{CO}^{-1} (interval 1) to 6.1 MWh t_{CO}^{-1} (interval 2) and 6 MWh t_{CO}^{-1} (interval 3). These results showcase the advantages of a (semi-)continuous feeding system, as the results remain rather constant over a longer period of time. During our experiments, the number of feeding cycles was limited to three, but they can be extended by supplying the carbon silo with a sufficient amount of carbon. Future experiments will focus on the effect of continuously feeding carbon into the carbon bed, to ensure a stable temperature inside the carbon bed, leading to less fluctuations in the CO concentration.

4.5. Post-plasma chamber modelling insights

To obtain better insight into the experimental results, we present in Fig. 13(a–d) the temporal evolution of temperature and CO concentration in the post-plasma chamber, as obtained from our model.

During the simulation time between 1 ms and 100 s, the carbon bed is observed to undergo significant changes in temperature, with a large corresponding change in the CO concentration in the post-plasma chamber, which is observed in Fig. 13. At 1 ms (Fig. 13a), the hot gas leaving the plasma reactor and injected into the post-plasma chamber (at z = 0 mm) begins to expand into the exhaust region. The gas temperature increases in the region close to the inlets to approximately 6000 K, which is consistent with our models of the plasma chamber described in the ESI† (section S3). At this time, the high-temperature gas has not yet reached the carbon bed, and thus the CO concentration is determined solely by the initial molar fractions. After 1 s (Fig. 13b), the gas reaches the carbon bed and the conversion of C_s to CO begins to occur. At this point, the average temperature in the bed remains low, as the impinging high temperature flow initially only heats the bed locally. In addition, the endothermic reaction occurring at these locations prevents the rapid propagation of the heat into the bed. As $C_{(s)}$ ablation proceeds at these locations, the molar fraction of CO starts to increase (to 10.4%) and plumes of CO can be seen exiting the carbon bed. At 10 s (Fig. 13c), the temperature in the carbon bed slowly increases, but most of the carbon bed

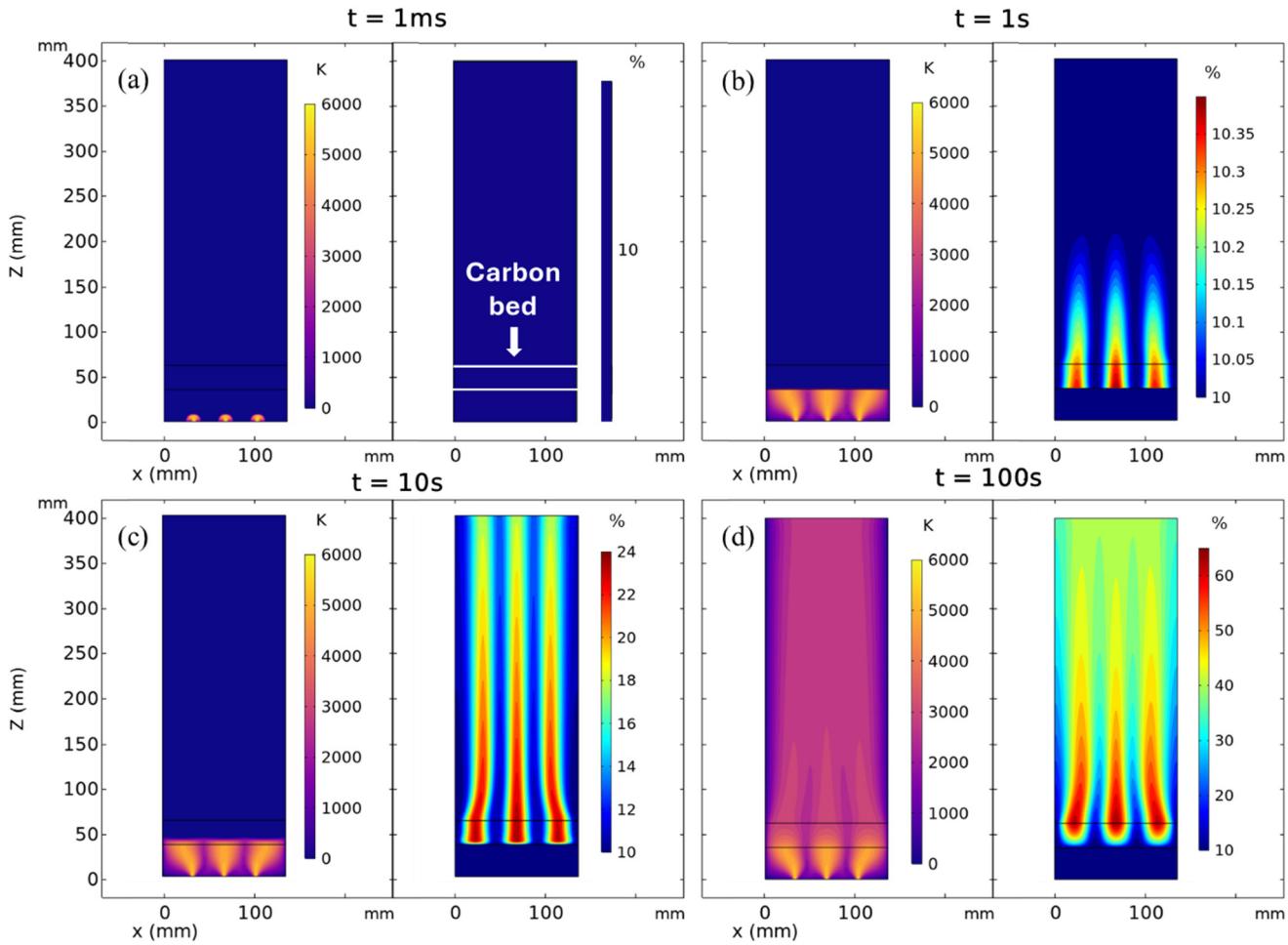

Fig. 13 Temperature (left panels) and CO concentration (right panels) in the post-plasma chamber, calculated at four different times: (a) 1 ms, (b) 1 s, (c) 10 s, and (d) 100 s. Inflow gas ratio of 90/10 CO_2/CO and carbon bed located in position 1 (35 mm from inlets), as indicated by the thin horizontal lines at z = 35 mm and z = 62 mm; see also Fig. 4 above.

remains at approximately 300 K. The CO plumes extend from the carbon bed to the end of the post-plasma chamber (simulation domain), with the maximum CO concentration doubling to a value of 24%. After 100 s (Fig. 13d), the calculated temperature has increased throughout both the carbon bed (porous medium) and the post-bed gas phase domain, reaching an average temperature of 3000 K. The CO concentration reaches a maximum of 62% in the carbon bed, with the plumes of formed CO diffusing across the post-bed chamber. This results in a nearly uniform CO concentration of 39% at the outlet, which aligns reasonably well with the experimental value of 25% at this time point (Fig. 5a), given the approximations in the model.

After 100 s, the CO production and outlet concentration begin to drop, as shown in Fig. 14a. The CO production rate at the C_s sites in the bed depends on both the gas temperature and pellet surface area (eqn (29)), with the former correlation demonstrated in Fig. 14a and b.

In the absence of a carbon bed, the CO concentration and temperature remain constant as a function of time due to the fact that gas phase recombination reactions are neglected in this ablation model. However, in the cases with a carbon bed, a dramatic increase in CO concentration occurs during the first 100 s as shown above, reaching values between 37 and 39% for all the bed positions. These peak values are consistent with experimental results shown in Fig. 5. After this point, the concentration in the model decreases linearly to approximately 32% over 3600 s (1 h). As mentioned above, the rate of CO production is dependent on the temperature and the carbon pellet surface area (eqn (29)). The initial rapid increase in CO concentration is associated with the increase in the carbon bed temperature during this time. The decrease observed after 100 s is primarily due to the decreasing size of the carbon pellets (Fig. S8†), reducing the rate of CO production. The averaged final diameter of the particles after 3600 s is 3.25 mm, meaning that the RBR rate will decrease by about a factor of 0.65. The increasing temperature profile after 100 s is correlated to a self-consistent calculation of the equilibrium properties of the bed. The thermal properties of the bed are determined assuming that the bed is in equilibrium with the gas, as defined in section 3.2.2. A reduction in the size of the pellets increases the proportion

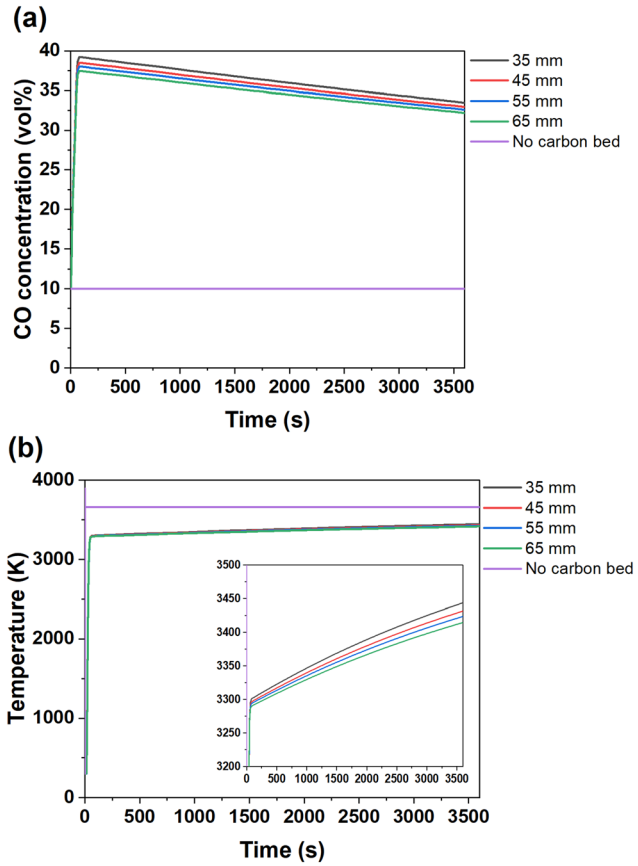

Fig. 14 Temporal average (a) CO concentration at the outlet and (b) bed temperature, for an inflow gas ratio of 90/10 CO_2/CO, and carbon bed located at different positions. Inset highlights the bed temperature change as a function of carbon bed position.

of gas in the bed. The solid carbon has a higher thermal conductivity and heat capacity than the gas, so an increase in proportion of the gas results in a higher temperature, and this is observed in the model from 100 s to 3600 s where the gas temperature increases by approximately 100 K for each bed position. A secondary contributing factor to this increase is the reduction in the endothermic rate of reaction that occurs due to the shrinking particles (eqn (11)). As the increase in temperature from 100 s to 3600 s has a smaller influence on the rate compared to the changes in magnitude of the surface area, the CO concentration decreases in this time period. This interplay highlights the importance of coupling the calculation of gas temperature, species production and gas flow through the bed.

While each bed position performs similarly, the exact location slightly influences the change in concentration over time, as predicted by our model. When the carbon bed is located closest to the inlets (*i.e.* 35 mm), the CO concentration increases in the first 100 s to a value of around 39%, decreasing to a value of 33% after 3600 s. In comparison, for the bed positioned furthest from the inlets (*i.e.* 65 mm), the value after 100 s is 37% and it drops to 32% at the end of the simulation. This difference in CO production is directly correlated to the average bed temperature, shown in Fig. 14b. When the carbon bed is located closer to the inlets, less conductive heat losses to the water-cooled walls occur and both the average bed temperature and CO production rate are elevated, as highlighted by the inset of Fig. 14b. This is consistent with previous experimental and modelling work,[4,12] where the observation of elevated bed temperature (either through higher power or closer coupling of the bed and plasma chamber) is beneficial for CO production. These results also demonstrate why the closer carbon bed position yields the best performance in our experiments.

While the multi-dimensional model described in this work is relatively simple, the conclusions that can be drawn align well with previous experimental and modelled observations. The model serves to highlight how the flow of gas through the bed influences the CO concentration detected at the outlet as a function of time, accounting for changes in the pellet size. Future work should include the influence of the gas flow rate and input power to the individual GAP reactors to demonstrate the flexibility of the model.

5. Conclusion

In this work, we have demonstrated that a post-plasma carbon bed can boost the performance of plasma-based CO_2 conversion on a pilot-scale level. The optimum performance was achieved with a carbon bed located closest to the plasma chamber (*i.e.* 35 mm downstream) at the lowest flow rate (50 L min^{-1}). With these parameters, the CO_2 conversion increased more than two-fold, from *ca.* 6% in the empty reactor to a peak value of 20% in the presence of carbon. This peak value correlates to the CO concentration at the outlet of 33 vol%. At this scale, the CO_2 conversion rate is 1068 g h^{-1} and the plug-based energy cost is 5.8 MWh t_{CO}^{-1} (1.2 MJ $mol_{CO_2}^{-1}$). To compare with literature values, which report plasma-based energy cost, this corresponds to a plasma-based energy cost of around 4.8 MWh t_{CO}^{-1} or 0.96 MJ $mol_{CO_2}^{-1}$. Although these values are higher than the best reported performance metrics reported for lab-scale setups,[12,13] they show the potential to apply a post-plasma carbon bed at an upscaled level, which has not been previously reported. Our experimental results show that a higher carbon bed temperature improves the performance due to the higher contribution of the RBR, which can be achieved by placing the carbon bed closer to the plasma reactor outlet(s). In addition, we show that real-time gas recycling in combination with the carbon bed enhances the conversion, albeit at the expense of the EC. Furthermore, we demonstrate how the improvement achieved with the batch system can be further enhanced with a semi-continuous carbon feeding system, reaching a peak CO_2 conversion of around 20% (33 vol% CO).

To gain deeper insights into the experimental results, we developed a 2D post-plasma chamber model for the carbon bed. Our model is a major improvement compared to previous 0D models, establishing for the first time a higher

dimensional carbon bed model. The model aligns well with experiments, showing that both the average bed temperature and outlet CO concentration increase when placed closer to the plasma chamber outlet. The combination of our experimental and modelling results displays the importance of bed temperature and the position of the carbon bed to maximize CO production in a pilot-scale MRGAP reactor.

Data availability

The authors hereby confirm that the data presented in this paper and the ESI† are safely stored on the server of the University of Antwerp and on a separate NAS drive of D-CRBN. The data can be retrieved at any time by contacting the corresponding author.

Author contributions

The manuscript was written through contributions of all authors. All authors have given approval to the final version of the manuscript.

Conflicts of interest

There are no conflicts to declare.

Acknowledgements

This research is financially supported by the VLAIO-Baekeland project (grant ID HBC.2023.0685) and the VLAIO-ICON project "BluePlasma", ID HBC.2022.0445. The authors would like to thank Anton Nikiforov (UGent, D-CRBN) for the interesting discussions and Amira Vandenbroucke (UAnwerpen, D-CRBN) for her assistance with the experimental work.

References

1 R. M. Cuéllar-Franca and A. Azapagic, *J. CO2 Util.*, 2015, **9**, 82–102.
2 R. Snoeckx and A. Bogaerts, *Chem. Soc. Rev.*, 2017, **46**, 5805–5863.
3 V. Vermeiren and A. Bogaerts, *J. Phys. Chem. C*, 2020, **124**, 18401–18415.
4 F. Girard-Sahun, O. Biondo, G. Trenchev, G. van Rooij and A. Bogaerts, *Chem. Eng. J.*, 2022, **442**, 136268.
5 D. S. Mallapragada, Y. Dvorkin, M. A. Modestino, D. V. Esposito, W. A. Smith, B.-M. Hodge, M. P. Harold, V. M. Donnelly, A. Nuz and C. Bloomquist, *Joule*, 2023, **7**, 23–41.
6 H. Conrads and M. Schmidt, *Plasma Sources Sci. Technol.*, 2000, **9**, 441.
7 A. Fridman, *Plasma chemistry*, Cambridge university press, 2008.
8 A. Bogaerts and G. Centi, *Front. Energy Res.*, 2020, **8**, 111.
9 S. Van Alphen, B. Wanten, F. Girard-Sahun, J. Slaets, J. Creel, M. Aghaei and A. Bogaerts, *ACS Sustainable Chem. Eng.*, 2024, **12**, 15715–15728.
10 D. C. van den Bekerom, J. P. Linares, T. Verreycken, E. M. Van Veldhuizen, S. Nijdam, G. Berden, W. A. Bongers, M. Van De Sanden and G. J. van Rooij, *Plasma Sources Sci. Technol.*, 2019, **28**, 055015.
11 P. Lahijani, Z. A. Zainal, M. Mohammadi and A. R. Mohamed, *Renewable Sustainable Energy Rev.*, 2015, **41**, 615–632.
12 O. Biondo, K. Wang, H. Zhang and A. Bogaerts, *Chem. Eng. J.*, 2025, 160190.
13 C. O'Modhrain, Y. Gorbanev and A. Bogaerts, *J. Energy Chem.*, 2025, **104**, 312–323.
14 H. Zhang, Q. Tan, Q. Huang, K. Wang, X. Tu, X. Zhao, C. Wu, J. Yan and X. Li, *ACS Sustainable Chem. Eng.*, 2022, **10**, 7712–7725.
15 J. Huang, H. Zhang, Q. Tan, L. Li, R. Xu, Z. Xu and X. Li, *J. CO2 Util.*, 2021, **45**, 101429.
16 Z. Li, T. Yang, S. Yuan, Y. Yin, E. J. Devid, Q. Huang, D. Auerbach and A. W. Kleyn, *J. Energy Chem.*, 2020, **45**, 128–134.
17 H. S. Uhm, H. S. Kwak and Y. C. Hong, *Environ. Pollut.*, 2016, **211**, 191–197.
18 Y. Wu, S.-Z. Li, Y.-L. Niu, H.-J. Yan, D. Yang and J. Zhang, *J. Phys. D: Appl. Phys.*, 2023, **56**, 065201.
19 L. Peng, L. Xuesong, S. Jun, Y. Yongxiang, Y. Tao, Q. Huang, D. Auerbach and A. W. Kleiyn, *Plasma Sci. Technol.*, 2018, **21**, 012001.
20 H. Liu, *Ammonia synthesis catalysts: innovation and practice*, World Scientific, 2013.
21 J. M. Modak, *Resonance*, 2011, **16**, 1159–1167.
22 R. Vertongen, G. Trenchev, R. Van Loenhout and A. Bogaerts, *J. CO2 Util.*, 2022, **66**, 102252.
23 M. Ramakers, G. Trenchev, S. Heijkers, W. Wang and A. Bogaerts, *ChemSusChem*, 2017, **10**, 2642–2652.
24 G. Trenchev, S. Kolev, W. Wang, M. Ramakers and A. Bogaerts, *J. Phys. Chem. C*, 2017, **121**, 24470–24479.
25 N. Pinhão, A. Moura, J. Branco and J. Neves, *ISPC2015-Proceedings*, Universiteit Antwerpen, 2015, pp. 1–3.
26 B. Wanten, R. Vertongen, R. De Meyer and A. Bogaerts, *J. Energy Chem.*, 2023, **86**, 180–196.
27 C. O'Modhrain, G. Trenchev, Y. Gorbanev and A. Bogaerts, *ACS Eng. Au*, 2024, **4**(3), 333–344.
28 S. Maerivoet, I. Tsonev, J. Slaets, F. Reniers and A. Bogaerts, *Chem. Eng. J.*, 2024, **492**, 152006.
29 S. Van Alphen, F. Jardali, J. Creel, G. Trenchev, R. Snyders and A. Bogaerts, *Sustainable Energy Fuels*, 2021, **5**, 1786–1800.
30 G. K. Batchelor, *An introduction to fluid dynamics*, Cambridge university press, 2000.
31 S. Van Alphen, H. A. Eshtehardi, C. O'Modhrain, J. Bogaerts, H. Van Poyer, J. Creel, M.-P. Delplancke, R. Snyders and A. Bogaerts, *Chem. Eng. J.*, 2022, **443**, 136529.
32 S. Maerivoet, B. Wanten, R. De Meyer, M. Van Hove, S. Van Alphen and A. Bogaerts, *ACS Sustainable Chem. Eng.*, 2024, **12**, 11419–11434.
33 K. Yang and R. Yang, *AIChE J.*, 1985, **31**, 1313–1321.
34 D. R. Stull, *JANAF Thermochemical Tables*, Clearinghouse, 1965.
35 R. Kars, R. Best and A. Drinkenburg, *Chem. Eng. J.*, 1979, **17**, 201–210.
36 D. Menard, X. Py and N. Mazet, *Chem. Eng. Process.: Process Intesif.*, 2007, **46**, 565–572.
37 I. Tsonev, C. O'Modhrain, A. Bogaerts and Y. Gorbanev, *ACS Sustainable Chem. Eng.*, 2023, **11**, 1888–1897.